J. Fluid Mech. (2002), *vol.* 468, *pp.* 327–347.
DOI: 10.1017/S0022112002001234 Printed in the United Kingdom

Forces on particles in oscillatory boundary layers

By PAUL F. FISCHER[1], GARY K. LEAF[1] AND JUAN M. RESTREPO[2]

[1]Mathematics and Computer Science Division, Argonne National Laboratory, Argonne, IL 60439, USA

[2]Mathematics Department and Program in Applied Mathematics, University of Arizona, Tucson, AZ 85721, USA

(Received 10 August 2001 and in revised form 1 April 2002)

The lift and drag forces on an isolated particle resulting from an oscillating wall-bounded flow, are approximated using direct numerical simulation and extrapolation techniques. We also confirm the existence of anomalies in the lift force, which arise from the interaction of the vortical field with the particle. Anomalies can also occur for computational reasons and these are discussed as well.

This study was motivated by a long-standing question about the importance of lift forces in the dynamics of sediments in oceanic settings. To answer this question we use the numerically generated data as well as extrapolations to compute the ratio of the lift to buoyancy forces on a particle. This analysis suggests that for particles and oceanic conditions typical of the nearshore, the lift force can play a role in the dynamics of sedimentary beds.

1. Introduction

The study of transport of precipitated and partially suspended particles in oscillatory wall-bounded flows, such as in the boundary layer of oceans, lakes and some rivers, is fundamental to understanding the dynamics of sediment, pollutants, and the motion of biogenic agents in these settings. In addition to its environmental implications, the study of transport in the boundary layer is also relevant to engineering issues in coastal environments, such as coastal erosion, the design and maintenance of off-shore structures, and the interaction of sea beds with buried pipes and transmission lines.

Two central issues in sediment transport are the processes of particle dislodgement and suspension. An understanding of these depend, at a fundamental level, on having a comprehensive picture of the quantitative and qualitative aspects of the forces resulting from the fluid on the particles, namely, lift, drag and buoyancy (see Sleath 1984; Fredsøe & Deigaard 1992 chapter 7; Nielsen 1992 chapter 2). Certainly, drag forces are important in initiating and maintaining bed load movement. Models for the formation and evolution of sedimentary beds, such as those appearing in Horikawa (1981), Dyer & Soulsby (1988), Fredsøe & Deigaard (1992), Restrepo & Bona (1995) and Restrepo (2001), crucially depend on the relationship between the flow velocity and the shearing of erodible beds. We would expect lift forces to be important in the dislodgement and suspension of particles. However, our present knowledge of fundamental aspects of these forces, even when consideration is limited to a single particle, is incomplete. We know little about forces on a single particle in an oscillating flow and thus about the contribution of the lift to the dynamics of the particle. We

know even less about the role played by the drag, lift and buoyancy forces in the dynamics of erodible beds containing many particles.

An understanding of lift and drag forces on particles is also important in a variety of chemical engineering and industrial applications. Interest in the geophysical as well as in the industrial problems has spawned a large number of studies, including Rubinov & Keller (1961), Saffman (1965), Hall (1968), Harper & Chen (1968), Dandy & Dyer (1990), Cherukat & McLaughlin (1993), Cherukat, McLaughlin & Graham (1994), Lovalenti & Brady (1995), Sakamoto & Haniu (1995), Mollinger & Nieuwstadt (1996) Niño & Garcia (1996), Wang *et al.* (1997), Kim, Elghobashi & Sirignano (1998), and Kurose & Komori (1999). In addition to these are Cox & Hsu (1977), Asmolov (1990) and McLaughlin (1993), in which estimates of the lift force on a particle neighbouring a bounding wall under the action of a steady flow are computed. Also of direct relevance is the asymptotic estimate in Asmolov & McLaughlin (1999) of the lift on a sphere in an oscillating linear shear flow.

A few laboratory measurements have been made of the drag on spheres placed in the neighbourhood of a wall subjected to oscillatory flows. Among them are those in Ponce-Campos & Brater (1985). Measurements of the lift and drag forces on isolated spheres in oscillatory flows, as well as of particles over packed beds, were reported in Rosenthal & Sleath (1986). To our knowledge, these are the only experimental studies to date. Rosenthal & Sleath (1986 referred to as RS hereinafter) is the inspiration behind this study. Our long-term objective is to understand the mechanics of particle suspension and dislodgement in wall-bounded oscillatory flows by numerical means, experiment and theory. A logical starting point is to measure the lift and drag forces of a single stationary particle sitting on the bottom wall in an oscillating flow. In doing so, we extend the lift measurements of RS to a larger parameter range than was practical at the time their study was performed.

Several constraints limited the experiments in RS. First, since typical sediment particles are small, the forces to be measured were difficult to resolve, the experiments were performed in a regime corresponding to gravel-sized particles, rather than typical sand-sized particles; secondly, practical constraints limited the parameter coverage of the experiments; thirdly, some of the measurements did not provide a qualitative description of certain aspects of the flow. These would have been useful in explaining certain experimental outcomes.

Here, we use numerical simulation of the Navier–Stokes equations for an incompressible fluid in three space dimensions to perform *ab initio* calculations of the forces on isolated particles, circumventing some of the issues in obtaining these forces through experiments or asymptotic analysis. Unlike the calculations of lift in oscillatory flows, such as those in Cherukat & McLaughlin (1993), Cherukat *et al.* (1994), Asmolov & McLaughlin (1999), ours are not restricted to order unity Reynods numbers or to disparate diffusive, convective and oscillatory length scales. Naturally, our calculations have practical restrictions on the range of the Reynolds number and the period of oscillation of the forcing. As we shall see, however, these restrictions accommodate a range of parameters corresponding to flows of physical importance and scientific interest.

In § 2, we describe the flow and its non-dimensionalization. The numerical methodology is presented in § 3. The results of the measurements are summarized in § 4. Section 4 also describes important new qualitative features of the flow particular to the setting under scrutiny. Section 5 discusses the implications of our results in the sediment dynamics setting, and § 6 summarizes our findings. The raw data appear in the Appendix.

2. Description of the flow

We consider the lift and drag forces on a spherical particle that is at rest on or near a bed of infinite extent when subjected to a wave-induced oscillatory boundary-layer flow. Assuming the direction of wave propagation to be x, and the bed-normal direction to be z, we describe the velocity profile, in the absence of a sphere, by

$$\hat{u} = U\left[\sin\left(kx - \frac{2\pi t}{T}\right) - \mathrm{e}^{-\beta z}\sin\left(kx - \frac{2\pi t}{T} + \beta z\right)\right], \tag{2.1}$$

where k is the wavenumber, T is the period of oscillation, and $\beta = \sqrt{\pi/\nu T}$, is the inverse Stokes-layer thickness. In the present study, we consider only the case of zero wavenumber.

We are interested primarily in flow conditions that occur in sediment transport generated by the action of nearshore surface waves. Thus, we focus on periods T in the range 1–15 s, particle diameters D no larger than 1.0 mm, and velocity amplitudes lower than about $1\,\mathrm{m\,s^{-1}}$. Simulations for parameters in these ranges are difficult to perform because of the spread in the scales required to resolve the flow; the number of advective time units required to resolve the period must increase with the period. For long periods, the number is substantial. Likewise, computations can become expensive because of the need to resolve several disparate length scales in the dynamics.

There are two length scales in the direction perpendicular to the bottom (wall). The first is determined by the particle diameter D. The second scale is determined by the oscillatory (Stokes) boundary layer, which is proportional to $\sqrt{\nu T}$. In the direction parallel to the wall, two length scales can be defined as well. One scale is again the diameter D; the other, associated with vortex formation, shedding and potential interaction, is determined by the period T and velocity U. For sinusoidal motion, this distance is roughly

$$L_{ex} = \frac{UT}{2\pi}, \tag{2.2}$$

corresponding to the excursion of a particle convected by the far-field base flow. (An ejected vortex ring can potentially travel further.) For long periods, L_{ex} is much greater than the scale D of the particle. Long periods require large enough domain sizes to allow disturbances (e.g. vortices) to propagate away from the particle. For moderate periods, it suffices to model the flow by using periodic boundary conditions in the direction parallel to the wall. In this case, the simulation domain does not have to be extremely large in order to avoid interactions between disturbances (periodic 'wrap-around'). For longer periods, domains based on the use of periodic boundary conditions become prohibitively expensive computationally.

Choosing the particle diameter D, velocity amplitude U and convective time D/U as respective characteristic length, velocity and time scales, we obtain the non-dimensionalized form of the Navier–Stokes equations

$$\frac{\partial \boldsymbol{u}}{\partial t} + \boldsymbol{u}\cdot\nabla\boldsymbol{u} = -\frac{1}{\rho_0}\nabla p + \frac{1}{Re}\nabla^2\boldsymbol{u}, \tag{2.3}$$

$$\nabla\cdot\boldsymbol{u} = 0. \tag{2.4}$$

Here, we assume that the independent coordinates (x, y, z, t) have been scaled by respective characteristic length and time scales. The Reynolds number,

$$Re \equiv UD/\nu, \tag{2.5}$$

is one of two independent parameters characterizing this flow. We choose as a second independent parameter the non-dimensional period

$$\tau \equiv TU/D, \tag{2.6}$$

which is also referred to as the Keulegan–Carpenter number. Another independent parameter is ϵ, which denotes the non-dimensionalized gap between the bottom of the sphere and the wall. In addition to these parameters, an important dependent parameter that characterizes the base flow is the non-dimensional Stokes-layer thickness

$$\delta \equiv \sqrt{\frac{\tau}{\pi Re}}. \tag{2.7}$$

Finally, when computing the potential response of the sphere to the lift and drag forces, we also must consider the ratio

$$\gamma \equiv \frac{\rho_0}{\rho - \rho_0},$$

which involves the density of the fluid, ρ_0, and the density of the particle, ρ.

Over each time cycle, we record the lift and drag force values. These values are then used to define the maximum and minimum lift and drag coefficients over each time cycle. These coefficients constitute the primary result from a given simulation. In the dimensional variables, we let F_x and F_z denote the drag and lift force, respectively. Then, the coefficients C_L and C_D are defined by

$$C_L = \frac{F_z}{\frac{1}{2}A\rho_0 U^2},$$
$$C_D = \frac{F_x}{\frac{1}{2}A\rho_0 U^2}, \tag{2.8}$$

where $A = \frac{1}{4}\pi D^2$ is the cross-sectional area.

3. Numerical approximation of the flow

Numerical solutions to (2.4) are based on the $\mathbb{P}_N - \mathbb{P}_{N-2}$ spectral element method, which is a high-order weighted residual technique that employs compatible trial and test spaces for the velocity and pressure (see Maday & Patera 1989; Fischer 1997). The computational domain is partitioned into K hexahedral elements, which may be deformed by using isoparametric mappings. Within each element, velocity and pressure are represented in local Cartesian coordinates by tensor-product Lagrange polynomials of degree N and $N-2$, respectively. C^0 continuity is enforced across element interfaces for velocity, while the pressure is allowed to be discontinous. At each time step, the momentum equations are advanced by first computing a convective substep, followed by a linear Stokes solve for the viscous and pressure terms. The pressure and velocity in the Stokes problem are decoupled through an additional time-splitting after discretization in space, such that *ad hoc* boundary conditions for pressure are avoided. The overall scheme is third-order accurate in time. Full details of the discretization and solution method may be found in Fischer (1997), Fischer & Mullen (2001) and Maday, Patera & Rønquist (1990).

The computational domain consisted of a rectangular volume with $x \in [-\frac{1}{2}L, \frac{1}{2}L]$, $y \in [0, -5.5]$, and $z \in [0, 7.8]$. For $\tau \leqslant 104$, periodic boundary conditions were imposed in the x direction. In this case, we must have $L > \tau/2\pi$ to ensure that

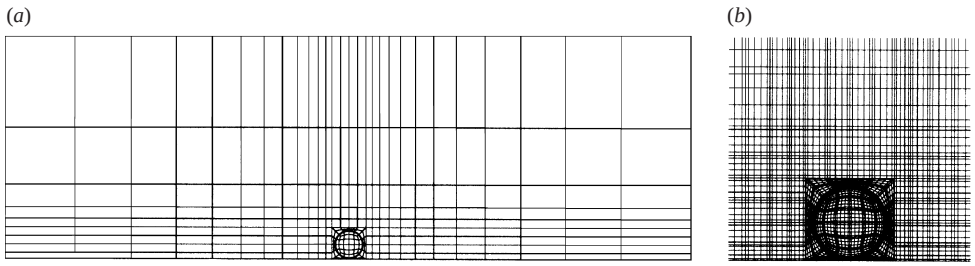

FIGURE 1. (*a*) Spectral element distribution in the symmetry plane of the short computational domain. (*b*) A close-up near the sphere showing the associated Gauss–Lobatto grid for $N = 5$.

vortices shed from the particle do not re-encounter the particle as they pass across the periodic boundary. We chose $L = 24$ for $\tau < 56$ and $L = 55$ otherwise. To reduce the computational costs, symmetry was imposed at $y = 0$. Experimental observations under similar conditions indicated that these flows should retain bilateral symmetry in the spanwise direction (see Acalar & Smith 1987). This assumption was validated by comparing lift versus time for the $(Re, \tau, \epsilon) = (500, 48, 0.0156)$ case with and without the symmetry assumption. Symmetry was also applied at $y = -5.5$ and $z = 7.8$, as this is a standard approach for imposing minimally invasive far-field boundary conditions. Homogeneous Dirichlet boundary conditions were applied on the wall at $z = 0$ and on the particle surface. The computational domain and its discretization are depicted in figure 1.

For the periodic case, the pressure is expressed as

$$p = \tilde{p}(x, y, z, t) + p_0(x, t), \qquad (3.1)$$
$$p_0 := \frac{2\pi x}{\tau} \cos\left(\frac{2\pi t}{\tau}\right),$$

where p_0 supplies the time-dependent mean pressure gradient, which drives the flow, and $\tilde{p}$ is the spatially periodic perturbation computed as the solution of the Stokes problem. The initial condition for the velocity is zero.

For large values of τ, it is difficult to avoid the effects of periodic wrap-around, that is, to have $L > \tau/2\pi$. This scale disparity would force us to use unusually large computational domains, which would be a drain on computational storage, as well as computational time, since the simulations become very long. To overcome these difficulties, we alternate inflow (Dirichlet) and outflow (Neumann) boundary conditions on each end of the domain in accordance with the predominant flow direction. This approach is reasonable under the assumption that vorticity carried sufficiently far from the particle does not return when the flow reverses. This will be true when there is sufficient time for decay or when vortices have a mild amount of forward progression. Therefore, for $104 \leqslant \tau \leqslant 400$, the initial and boundary conditions at $x = \pm\frac{1}{2}L$ are based on the non-dimensional form of (2.1), and the forcing term p_0 is set to zero. The lift versus time for this approach was compared with the periodic results at $\tau = 104$. No discernible difference was detected.

The process of generating and obtaining the lift and drag datum is described as follows. Unless otherwise indicated, all simulations start with zero initial conditions. The oscillatory forcing is impulsively started at this initial time. Each simulation is run until a steady pattern in the lift emerges. For large periods ($\tau > 10$), this typically occurs in fewer than six cycles. We note that, while it is tempting to use the settled

Re	C_{LT}		C_{LV}		C_{LP}	
50	0.111	0.105	0.060	0.057	0.051	0.048
100	0.078	0.074	0.036	0.033	0.042	0.041
150	0.088	0.080	0.032	0.029	0.056	0.051

TABLE 1. Comparison of lift coefficients as a function of the Reynolds number Re with the data from Kim *et al.* (1998) (left-hand columns) and present (right-hand columns).

flow field for one value of τ as the initial condition for the next, such a restart approach can lead to spurious results. This point is discussed further in § 4.

For the production simulations, the polynomial degree was $N = 5$. Convergence was checked by comparing the lift results with those obtained with $N = 7$ for the particular case $(Re, \tau, \epsilon) = (300, 16, 0.25)$. For the short-domain simulations, the number of spectral elements was $K = 1828$, corresponding to 234 359 velocity points and 116 992 pressure points. For the longer domains, we used $K = 2836$, corresponding to 362 339 velocity points and 181 504 pressure points. The simulations were performed on a eight-node Compaq Linux cluster with 500 MHz Alpha processors, using MPI for internode communication. The $(Re, \tau, \epsilon) = (300, 1, 0.0156)$ case required 80 time steps and approximately 15 CPU-minutes per period. For $(Re, \tau, \epsilon) = (100, 400, 0.0156)$, the number of steps per period was 66 667, and the simulation time was 3.7 days per period.

4. Lift and drag measurements

We describe here some qualitative aspects of the computed lift and drag forces. We first present results of benchmark calculations that are aimed at establishing confidence in the numerical approach.

4.1. *Benchmark calculations*

Two benchmark calculations were performed. In the first, we computed the lift forces on two spheres in a three-dimensional steady flow, following Kim *et al.* (1998, referred to as KES hereinafter). In the second, we compare the calculations of the lift to experimental data obtained by Rosenthal & Sleath in their oscillatory flow rig.

The physical set-up of KES was two spheres, sitting side by side with a gap between them. The steady flow was normal to the axis connecting the centres of the spheres. This situation was mimicked in the present code by changing the boundary condition on the wall to a symmetry condition, setting the boundary condition at $x = -\frac{1}{2}L$ to unit inflow and the boundary condition at $x = \frac{1}{2}L$ to outflow. Table 1 shows a comparison of the present calculations for the case $\epsilon = 0.25$ with those in KES. The KES data was obtained from their figure 11, p. 481. The table shows close agreement for the total lift coefficient (C_{LT}) and its constituent viscous (C_{LV}) and pressure (C_{LP}) contributions.

The comparison with the oscillatory data of RS is also for the case with $\epsilon = 0.25$. The Reynolds number is varied while the Stokes-layer thickness is kept fixed such that $\beta D = 14$. The maximum and minimum lift coefficients as a function of Re are plotted in figure 2. The dashed lines represent the computed coefficients, whereas the solid lines connect the values obtained from figure 7, p. 457 of RS. Because of practical considerations, the range of the simulated data does not reach beyond $Re \approx 1000$.

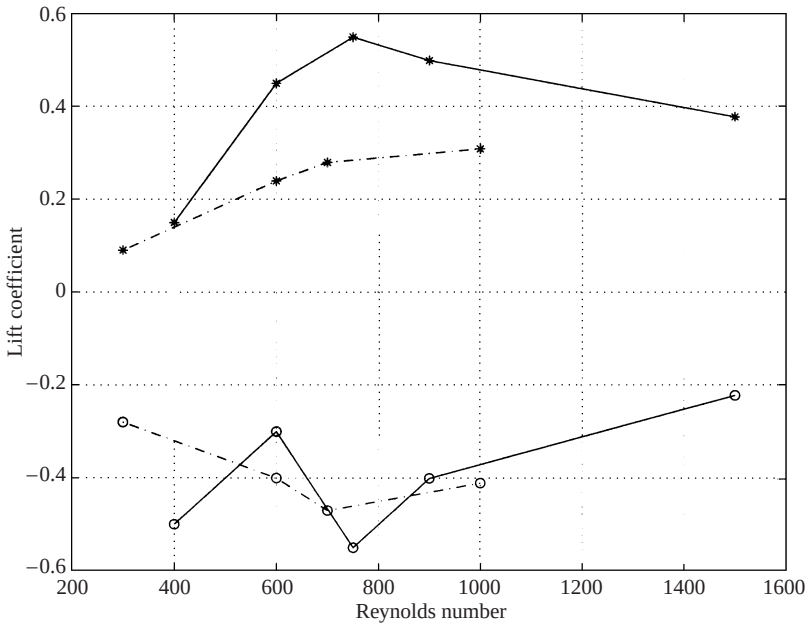

FIGURE 2. Maximum and minimum lift coefficient as a function of the Reynolds number, with $\beta D = 14$ and $\epsilon = 0.25$. Solid lines connect laboratory data from RS dashed lines computed data.

Although the simulated data compare favourably, there are significant discrepancies in the maximum lift coefficient for the larger Reynolds numbers.

A number of issues prevented a detailed comparison over the full range of the RS data, which extended to $Re = 5000$. First, because βD is fixed in the RS experiments, the period must grow in proportion to the Reynolds number. Thus, increasing the Reynolds number not only calls for higher resolution in the numerical computations (because of the usual increase in range of scales, lack of dissipation, etc.), it also requires larger domains in order to avoid periodic wrap-around, and longer simulation times owing to the longer period. Secondly, as noted in RS, the experimental data suffer from a low signal-to-noise ratio at lower Reynolds numbers, which makes it difficult to obtain measurements in the range which is readily accessible numerically. In fact, it was in part to circumvent these difficulties that we decided to fix Re and to vary τ in the present study.

4.2. *Qualitative aspects of the lift and drag*

We computed lift and drag for three Reynolds numbers, $Re = 100$, 300 and 500, each for a range of periods $\tau = 1$–96. In addition, coefficients for $\tau = 200$ were computed at $Re = 100$ and 500, and for $\tau = 400$ at $Re = 100$. The complete data are given in the Appendix.

The gap between the sphere and the solid surface is itself another parameter in the flow. How the lift and drag forces depend on the gap size will not be considered here, deferring consideration of this question to another study. Unless otherwise noted, the gap width in all cases is $\epsilon = 0.0156$, corresponding to a case considered in RS, hereinafter referred to as the 'zero gap' case.

Figure 3 (upper right-hand corner) shows the lift coefficient versus time for the case $(Re, \tau) = (300, 24)$ over a single cycle after the flow has reached a persistent periodic state. Similar lift versus time curves yield the minimum and maximum lift

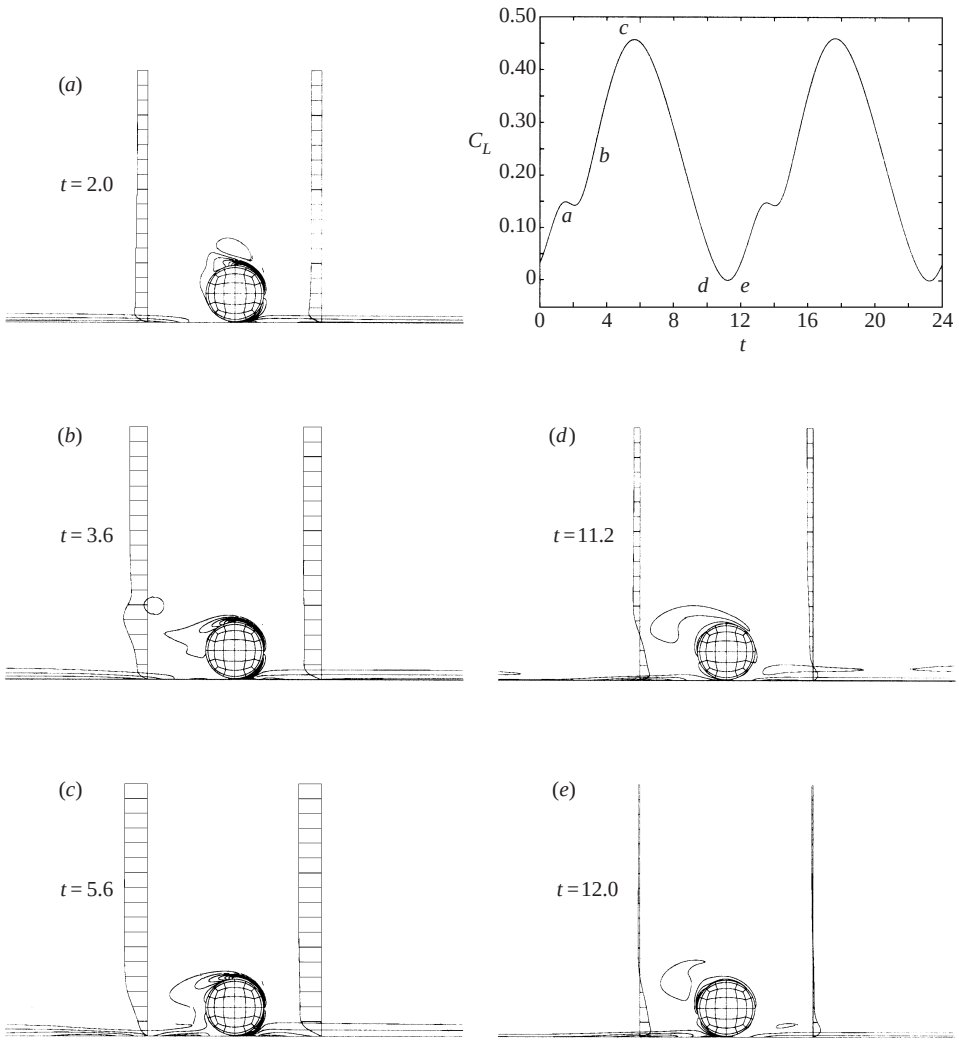

FIGURE 3. Lift coefficient as a function of time, upper right-hand corner, and corresponding vorticity distribution and velocity profiles at $x = \pm 1.5L$. $\tau = 24$, for $Re = 300$ and $\epsilon = 0.0156$.

coefficients for each (Re, τ) pair. The results shown are typical in that the lift exhibits a period that is half that of the driving period. Because of symmetry, the lift is the same whether the base flow is in the positive or negative x-direction. Also shown are selected plots of spanwise vorticity contours in the $y = 0$ plane, along with velocity profiles at $x = \pm 1.5$. We note that the maximum lift roughly coincides with the maximum base flow (c) and not with the point of vortex formation/ejection (a). In frame (b), we see that the ejected vortex has a significant impact on the base profile. Also visible in frame (a) is the 'toe' associated with the Stokes layer, in this case, at a height of roughly $y = 0.2$. Frames (d) and (e) show the flow conditions near the point of minimum lift. We note that this occurs when the far-field flow is nearly zero, while the near-wall flow has a non-trivial component. Thus, on the top of the sphere, the pressure is essentially the stagnation pressure, while on the bottom it is lower because of the Bernoulli effect. Note that in frames (d) and (e) the flow reversal associated

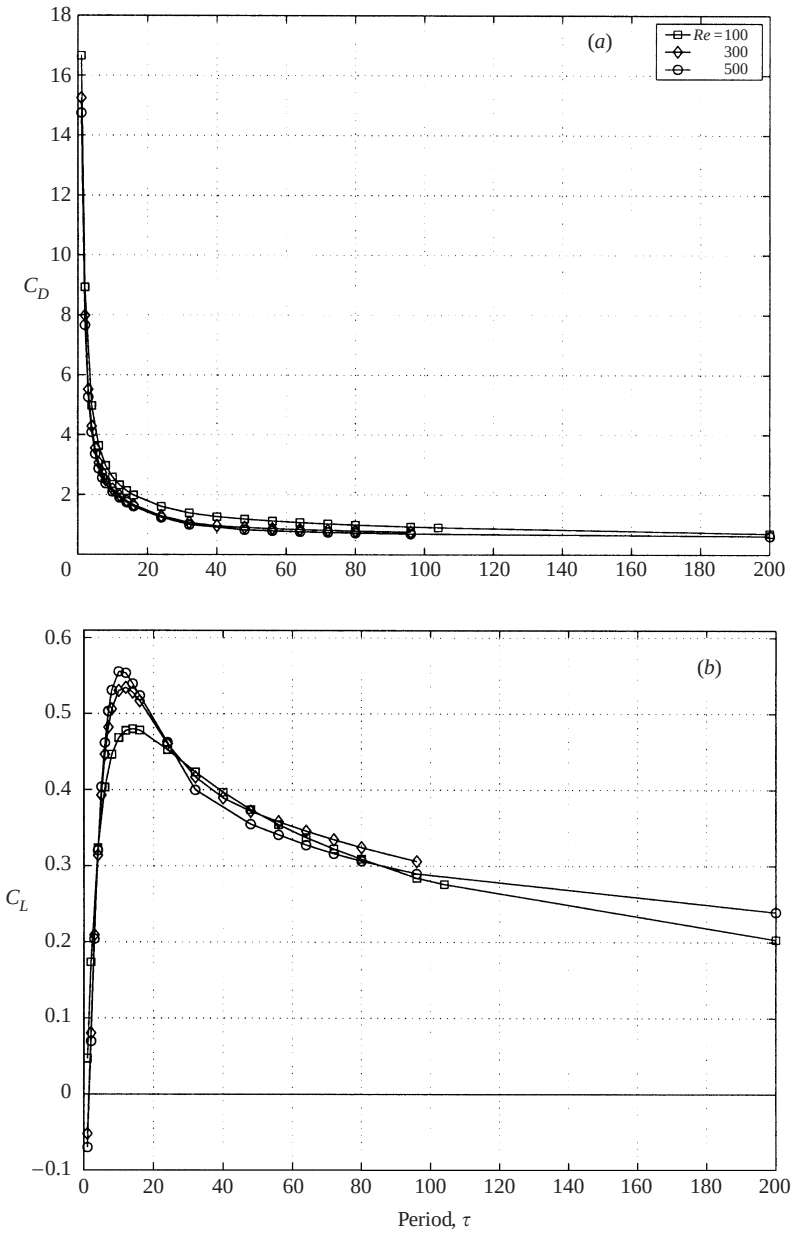

FIGURE 4. (*a*) Maximum drag coefficient, (*b*) maximum lift coefficient, as a function of period, for $Re = 100$, 300, 500. Not shown: maximum drag coefficient at $Re = 100$ for $\tau = 400$ is 0.5097, and maximum lift coefficient at $Re = 100$ for $\tau = 400$ is 0.1405.

with the alternating external pressure gradient (p_0) is significantly enhanced in the wake of the sphere, as a result of the momentum deficit there.

In figure 4(*a*), we plot the peak drag coefficient as a function of the period for each of the Reynolds numbers considered. We note that the peak lift is not strongly dependent on the Reynolds number over the range of values considered. The curves are approximately hyperbolic, with C_D approaching infinity as τ tends to zero. This is because the externally applied driving pressure, p_0, scales as τ^{-1} (3.1). Over the

range of periods considered, the lowest computed drag coefficient was $C_D = 0.5097$, corresponding to $Re = 100$, $\tau = 400$, for which the Stokes-layer thickness is $\delta = 0.886$, as computed from (2.7). In the limit $\tau \to \infty$, the drag coefficient must tend to zero, because the Stokes-layer thickness scales as $\sqrt{\tau/Re}$ and thus the velocity near the particle scales as $\sqrt{Re/\tau}$. In this Stokes limit, the drag force scales linearly with the near-particle velocity. Because the drag coefficient has U^2 in the denominator, we obtain $C_D = O(1/\sqrt{Re/\tau})$.

In figure 4(b), we plot the maximum lift coefficient as a function of τ. As in the case of the drag, the dependence of lift on Re is mild. Also, for all values of (Re, τ) considered, we have $C_L < C_D$. In contrast to the drag coefficient, the peak lift exhibits a local maximum in the interval $10 \leqslant \tau \leqslant 20$. In addition, the peak lift is negative for very small values of τ. The explanation for these features lies in the role of vortex formation in the wake of the particle. For short periods, $\tau < 10$, there is insufficient time for a significant vortex to form behind the particle. This time can be estimated if we assume that the length of a growing vortex is roughly half of the distance travelled by a particle in the free stream. As shown in Honji & Taneda (1969), the time evolution of the wake behind a cylinder exhibits a similar behaviour. Choosing a characteristic vortex size of unity, we require the particle excursion amplitude to be $L_{ex} = \tau/2\pi \simeq 2$, from which we conclude that $\tau > 12$ for vortex formation to become important. For very small values of τ, there is no time for viscous effects to become important, and the pressure field is thus dominated by potential flow effects. In this case, the flow is accelerated as it moves around the sphere, with a greater degree of acceleration (and higher velocity) arising between the sphere and the wall than occurs over the top of the sphere. Consequently, we can expect negative lift at all points in the cycle because of a Bernoulli effect. However, as τ increases, the gap region is the first to suffer the effects of viscocity, which includes the build-up of a vortex in the wake of the particle. As the size of the vortex increases with τ, the peak lift increases up to the point where the vortex is strong enough to detach from the particle during flow reversal. Finally, as τ approaches infinity, we expect C_L to vanish, following the Stokes-layer argument above for C_D. In this case, however, we anticipate that the convergence will be faster than $O(1/\sqrt{Re/\tau})$ since symmetry arguments imply that Stokes flow can produce zero lift under these conditions. We revisit this point in § 6.

To further understand the relationship between the peak lift and the period, we plot in Figure 5(a) the phase of the peak minimum and maximum C_L as a function of τ for $Re = 100$. Velocity profiles over the corresponding phase interval are shown in figure 5(b). The phase of the maximum C_L crosses the 90° mark at approximately the point corresponding to the lift peak in figure 4(b). For shorter periods, the phase lags the 90° mark, indicating that peak lift occurs after the peak in the base velocity, whereas for longer periods, the peak lift occurs prior to the peak in the base velocity. The minimum lift curve, corresponding to the minimum peak in the lift, exhibits a similar trend. The phase crosses the 0° degree mark at the same period value. For short periods, the minimum lift occurs after the change in the base-flow direction, whereas for longer periods it occurs prior to the change in flow direction.

Figure 6(a) shows the evolution of the total lift with time, as well as the relative strength of the viscous and pressure contributions, for the case $Re = 300$, $\tau = 3$ and $\epsilon = 0.25$. As the flow settles to a steady-periodic state, the particle experiences a lift force with a repetition rate that is twice the forcing frequency. For symmetric flow

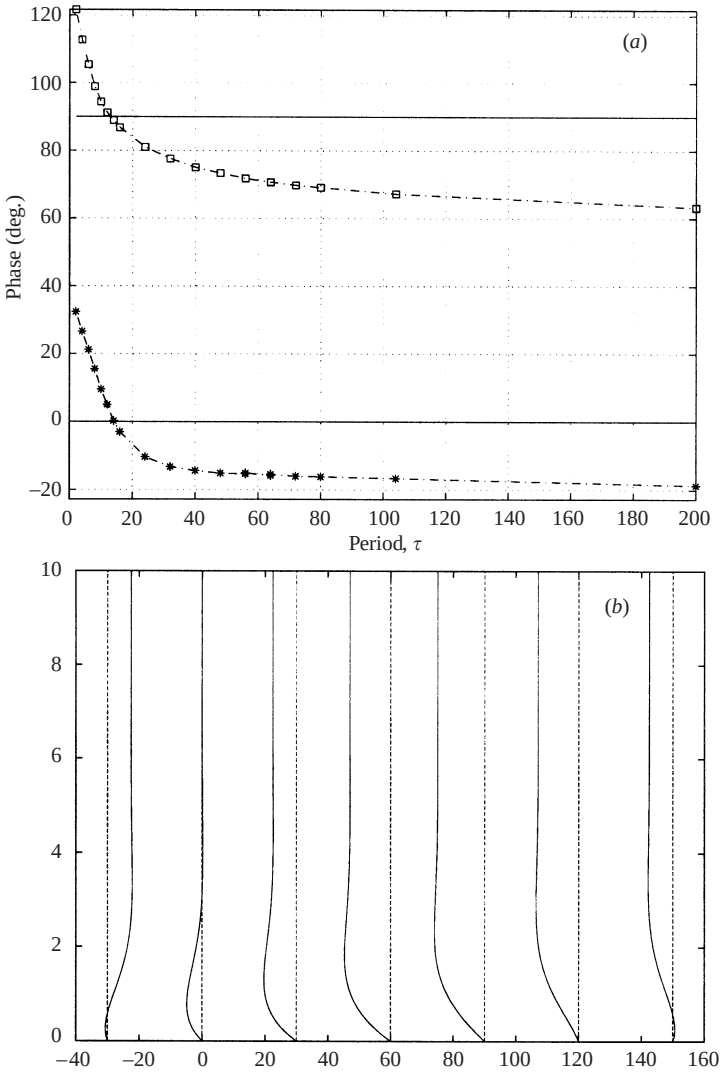

FIGURE 5. (*a*) Phase (degrees) of the peak *, minimum and □, maximum lift with respect to the forcing as a function of τ, for $Re = 100$; (*b*) velocity profile as a function of phase.

patterns, two peak events occur because the lift is insensitive to the direction of the flow. This is unlike the drag force, which will have a repetition rate that matches the forcing frequency. For small values of τ the time average of the lift typically is negative. Clearly, the Bernoulli mechanism that gives rise to the negative lift must also be a function of the gap size. In fact, when the gap is small and the frequency of forcing is sufficiently high, the particle can experience a negative lift, for all time, as recorded in figure 4(*b*).

Lift signals may also occur with a repetition rate that matches the forcing frequency. One such case is shown in figure 6(*b*), which indicates a non-symmetric flow pattern. The flow parameters (Re, τ, ϵ) for figures 6(*a*) and 6(*b*) are the same. The difference between these two cases is the choice of initial condition: in figure 6(*a*), the initial fluid velocity was zero, whereas in figure 6(*b*), the initial velocity field was non-zero.

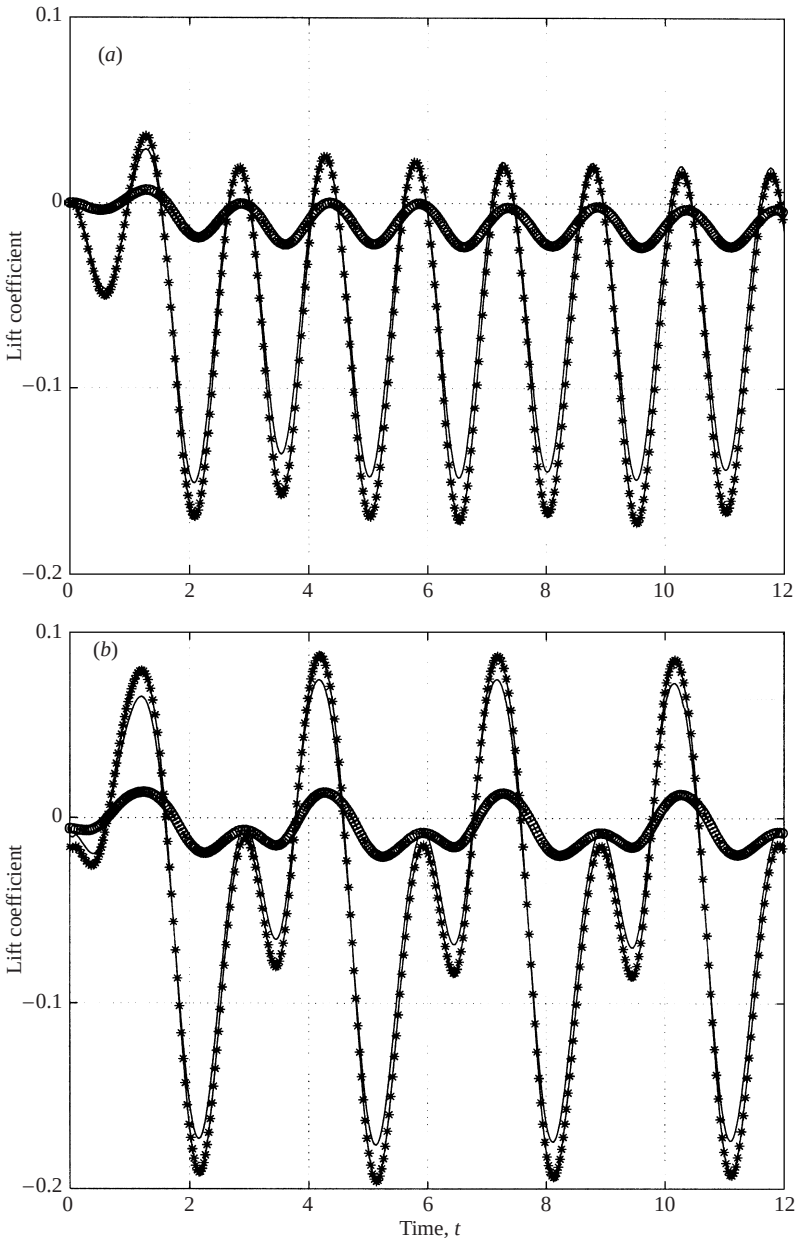

FIGURE 6. Time dependence of the lift coefficient: (*a*) zero initial condition, (*b*) non-zero initial condition. $Re = 300$, $\tau = 3$ and $\epsilon = 0.25$. *, total; ○, viscous; ——, pressure.

These calculations indicate that initial conditions can play a significant role in the magnitude and shape of the lift data sets. The effect can be a transient phenomenon, but the case highlighted clearly shows it as a persistent condition. Although the flow that leads to the anomaly in the lift was generated numerically, it is not ruled out as a physically realizable flow. In fact, it was not difficult to set up numerically. It arose in a sequence of computations in which we used a non-zero initial condition. Figure 7 shows lift coefficients as a function of the period, for $Re = 300$ and $\epsilon = 0.25$.

Re	γ	B	$C_L(\tau_s)$	Error
100	0.6185	1.0000	0.4236	1.4×10^{-3}
300	0.9950	0.5244	0.4171	1.3×10^{-3}
500	0.9519	0.5676	0.4001	1.6×10^{-3}

TABLE 2. Optimal parameters for a least-squares fit of (6) to the lift datum for $Re = 100$.

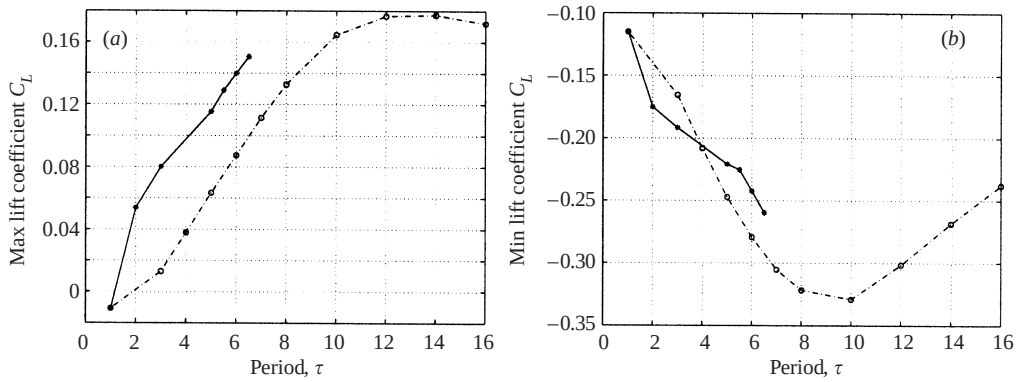

FIGURE 7. (a) Maximum and (b) minimum lift coefficient as a function of period τ, for $Re = 300$ and $\varepsilon = 0.25$.

Figure 7(a) plots the positive total lift coefficient and figure 7(b) the negative total lift coefficient. The dashed curves represent the lift coefficient calculated with zero initial conditions. The solid curves, on the other hand, are the result of using the solution from the simulation at the previous value of τ as the initial condition. An examination of the vorticity field corresponding to the solid curve calculations revealed that these cases exhibit vortex trapping, in which a strong vortex (generated under prior flow conditions) remains on one side of the particle throughout the cycle, giving rise to an asymmetric flow pattern and the anomalous lift curves shown in figures 6 and 7.

4.3. *Extrapolation and interpolation*

To extend the present study to a wider range of parameters Re and τ, we use extrapolation and interpolation. The extrapolation of force datum in τ and interpolation in Re will be described here and used later in order to consider the relevance of the lift force to a problem of physical interest.

We first describe the extrapolation procedure for the lift force calculation. From figure 4, we observe that each lift curve is characterized by a tail region where the lift coefficient decays monotonically as a function of τ. Let τ_s denote a value of τ in the vicinity of peak C_L. We define the tail region by $\tau \geqslant \tau_s$. Based on the data, we make a reasonable choice of $\tau_s = 32$, beyond which the behaviour of the curves is qualitatively similar for all curves, corresponding to the three Reynolds numbers. Let τ_f denote the final τ considered (i.e. $\tau_f = 104$ for $Re = 100$; $\tau_f = 96$ for $Re = 300$ and 500). For each curve, we fit the lift data in this tail region to the rational function $F(\tau, Re)$, given by

$$F(\tau, Re) = C_L(\tau_s)\left[1 - B + \frac{B}{(1+s)^{\gamma}}\right], \tag{4.1}$$

where $s = (\tau - \tau_s)/(\tau_f - \tau_s)$, and $C_L(\tau_s)$ is the lift coefficient at τ_s.

Re	τ	Extrapolation	Simulation	Relative error (%)
100	200	0.2011	0.2032	1.1
100	400	0.1382	0.1405	1.6
500	200	0.2396	0.2394	0.1

TABLE 3. Comparison of extrapolated and simulated values for the lift.

In table 2 we present the optimal fit parameters B and γ for each value of Re. The table also shows the mean-square error between the functional form (4.1) and the computed data, which provides a measure of the quality of the fit. The extrapolation is performed on the data for each Reynolds number. This is required because it is clear from the data that the lift coefficient curves are not self-similar in $\tau - Re$ space. Hence, for each Re, there is a different function F. The functions $F(\tau, Re)$ are used to extrapolate the lift data for larger values of τ. As a check on the quality of the extrapolation we computed lift/drag data for large values of τ. In the case of $Re = 100$, we calculated at $\tau = 200$ and 400. For $Re = 500$, we calculated at $\tau = 200$. The comparisons are shown in table 3. Based on these comparisons, we conclude that for moderate τ we can use the extrapolation to estimate the lift coefficient for points outside of the computed range.

5. Discussion

We now turn to the question first posed in Rosenthal & Sleath (1986), namely, how important lift forces are to sediment dynamics in the nearshore zone of the ocean. We will revert to dimensional quantities, as these will help convey a more concrete physical picture of the implications of the analysis. To make this assessment, we compare the relative strength of the lift force to the buoyancy force.

For a given particle with diameter D and density ρ, in a time-harmonic flow characterized by (T, U, ρ_0), the maximum lift force and the buoyancy force acting on the particle are given by

$$F_L = \tfrac{1}{2}\rho_0 A U^2 C_L$$

and

$$F_g = (\rho - \rho_0) g V,$$

where $V = \frac{1}{6}\pi D^3$ is the volume and $A = \frac{1}{4}\pi D^2$ is the cross-sectional area of the spherical particle. Here, g is the acceleration due to gravity. The ratio is given by

$$R_{Lg} = \frac{3\rho}{4(\rho - \rho_0)g} \frac{U^2}{D} C_L(Re, \tau). \tag{5.1}$$

For specificity, we take the fluid as water; hence, $\nu = 10^{-6}\,\mathrm{m^2\,s^{-1}}$, and $\rho_0 = 10^3\,\mathrm{kg\,m^{-3}}$. Having sand particles in mind, we use $\rho = 2.65\rho_0$, which roughly corresponds to the density of quartz. For convenience, we set $d = 10^{-3}D$, so that d is measured in millimetres, and $Re = 100r$. Then, from (2.5)–(2.6), the scaling relations take the form

$$\begin{aligned} d &= r/10, \\ T &= (\tau/100r)d^2, \end{aligned} \tag{5.2}$$

and the lift to buoyancy ratio takes the form

$$R_{Lg} \approx 1.23 \frac{r^2}{d^3} C_L(r, \tau). \tag{5.3}$$

If we were to rely exclusively on the direct measurements of $C_L(r, \tau)$, the range of flows and particle sizes not only would be limited, but also could fall in a regime of little physical interest. For example, consider the applicability of the data set measured for a flow with $Re = 100$ and $\tau = 96$. In this case, we measured $C_L = 0.2842$. For which flows (T, U) and particles d would this lift data be applicable? From (5.2), we see that (T, U, d) must satisfy the relations $Ud = 0.1$ and $T = 0.96d^2$. Suppose we consider flows with a period of 4 s. Then the data set applies to a particle with diameter $d = 2.04$ mm and a flow with $U = 0.05\,\mathrm{m\,s^{-1}}$ (about $2\,\mathrm{in\,s^{-1}}$). The corresponding value for $R_{Lg} = 0.03$. This is not a useful result, because we would not expect the lift force to be an important factor for such gravel-sized particles under these flow conditions. Suppose instead we start with a sand-sized particle, say $d = 0.5$ mm, and ask, 'For what flow conditions (T, U) does the same lift data set apply?' The period would be approximately 0.24 s. Without pursuing the matter further, we observe that wave periods this small are not relevant for nearshore sediment transport. This is yet another example that illustrates the limited applicability of the computed data to an oceanic setting.

As will be shown presently, other parameter limitations to the data exist. However, the range restrictions are obviated, to a certain degree, by the extrapolation procedure described in § 4.3. With the use of the extended values for C_L, we can explore a somewhat larger portion of (T, U, d) parameter space.

We first determine the portion of (T, U, d) space where the extended datum can be applied. Here, we use the particle diameter as a parameter and display the restrictions on U and T in terms of d. First, we consider the restriction on flow velocity resulting from the range of Reynolds numbers used in the simulations. We observe from (5.2) that we are restricted to flow velocities U for which

$$\frac{1}{10d} \leqslant U \leqslant \frac{1}{2d}, \tag{5.4}$$

in units of $\mathrm{m\,s^{-1}}$. For example, in the case of fine sand, $d \approx 0.25$ mm, the velocity range is restricted to $U \in [0.4, 2]\,\mathrm{m\,s^{-1}}$. For coarse sand, $d = 1.0$ mm, the velocity range shifts to $U \in [0.1, 0.5]\,\mathrm{m\,s^{-1}}$. The whole velocity range for the smaller particle is unrealistically high for nearshore wave conditions. For the coarser sand particle, however, the range is reasonable for these nearshore conditions.

Next we consider the restrictions on the period T. From (5.2) we find that

$$\frac{\tau d^2}{500} \leqslant T \leqslant \frac{\tau d^2}{100}. \tag{5.5}$$

As noted, without the use of extrapolation, this relation would severely restrict the periods for which the data are applicable. For example, with $d = 1.0$ mm and $\tau = 96$, T would be restricted to $T < 0.96$ s. For nearshore flow conditions, we expect periods in the range 1–15 s. Thus, for $d = 1.0$ mm, corresponding to coarse sand, values for the lift at $\tau = 800$ would provide a range for the period $T \in [1.6, 8]$ s. When fine sand ($d = 0.25$ mm) is considered, then in order to consider a wave with period $T = 8$ s, we would need lift data corresponding to $\tau = 12\,800$. Such large values for τ are well beyond the capability of direct numerical simulations.

As noted earlier, we verified that extrapolations of C_L out to $\tau = 400$ agreed with

d (mm)	T (s)	U ($\mathrm{m\,s^{-1}}$)
0.25	[0.06, 2.50]	[0.40, 2.0]
0.50	[0.24, 10.0]	[0.20, 1.0]
0.75	[0.54, 22.5]	[0.13, 0.67]
1.00	[0.96, 40.0]	[0.10, 0.50]

TABLE 4. Accessible regions of T–U space using extrapolation.

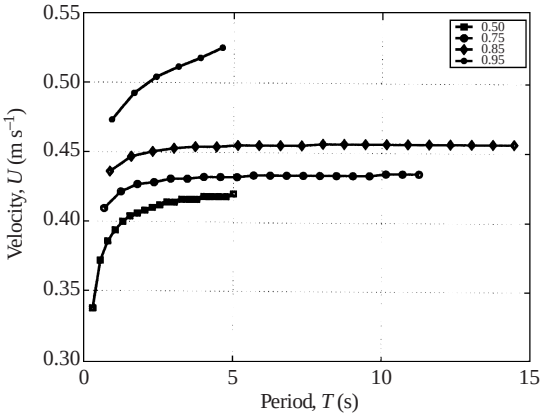

FIGURE 8. $R_{Lg} \approx 2.0$ contours for particle sizes $d = 0.50$–0.95 mm.

direct simulations to within 1–2%. Based on this observation, let us consider $\tau = 4000$ as an upper limit on the non-dimensional period. Table 4 shows the regions in the (T, U)-plane for the extrapolation data for a given particle diameter. The qualitative particle ranges are medium for ≈ 0.25 mm, coarse for 0.50 mm and very coarse for 1.00 mm. The table reiterates the fact that for small particles, the accessible range of velocities is higher and the range of periods is lower than would be typical of the oceanic setting. Even this moderate choice for peak τ, however, allows us to consider the importance of lift for medium- and larger-sized sand particles. Thus, we are able to extend the range of particle sizes considered by RS.

When comparing the relative importance of the lift force with the buoyancy force, we would like to determine what range of (T, U), for a given particle size, leads to an R_{Lg} which reflects the dominance of the lift force over the buoyant force. We are not concerned as much in determining exactly what velocities lead to R_{Lg} greater than one, but instead, whether for a given particle size there is a range of velocities of comparable magnitude to those found in the oceanic setting, that lead to a dominance of the lift force over the buoyant force. To this end, we plot the values of $R_{Lg} \approx 2.0$ in figure 8 for d in the range 0.50–0.95 mm. The region below each curve corresponds to $R_{Lg} < 2$. For smaller particle sizes, an obvious reduction in the velocity is required to achieve $R_{Lg} = 2$.

Finally, we can relate the estimates on the ratio of the lift to buoyancy force to wave conditions prevalent in the nearshore. Gravity waves obey a dispersion relation of the form

$$\omega^2 = gk \tanh(kh), \tag{5.6}$$

where k is the wavenumber of the waves, and ω is the frequency. These waves are

τ	Min. lift	Max. lift	Left drag	Right drag
1.0000	−0.2589	0.0472	−16.6552	16.6593
2.0000	−0.2152	0.1735	−8.9285	8.9256
4.0000	−0.1754	0.3235	−4.9743	4.9741
6.0000	−0.1197	0.4034	−3.6347	3.6345
8.0000	−0.0682	0.4465	−2.9751	2.9751
10.0000	−0.0288	0.4683	−2.5858	2.5857
12.0000	−0.0022	0.4779	−2.3244	2.3239
14.0000	0.0133	0.4801	−2.1325	2.1317
16.0000	0.0209	0.4782	−1.9835	1.9822
24.0000	0.0176	0.4527	−1.6046	1.6030
32.0000	0.0036	0.4236	−1.3943	1.3912
40.0000	−0.0077	0.3971	−1.2725	1.2665
48.0000	−0.0152	0.3744	−1.1914	1.1842
56.0000	−0.0197	0.3547	−1.1293	1.1216
64.0000	−0.0223	0.3376	−1.0796	1.0693
72.0000	−0.0235	0.3226	−1.0353	1.0277
80.0000	−0.0239	0.3093	−0.9978	0.9903
96.0000	−0.0236	0.2842	−0.6438	0.9276
104.0000	−0.0235	0.2760	−0.9050	0.9051
200.0000	−0.0145	0.2032	−0.6989	0.6989
400.0000	−0.0069	0.1405	−0.5105	0.5097

TABLE 5. For a given period τ, maximum and minimum lift over a cycle, maximum left and right drag over a cycle. $Re = 100$.

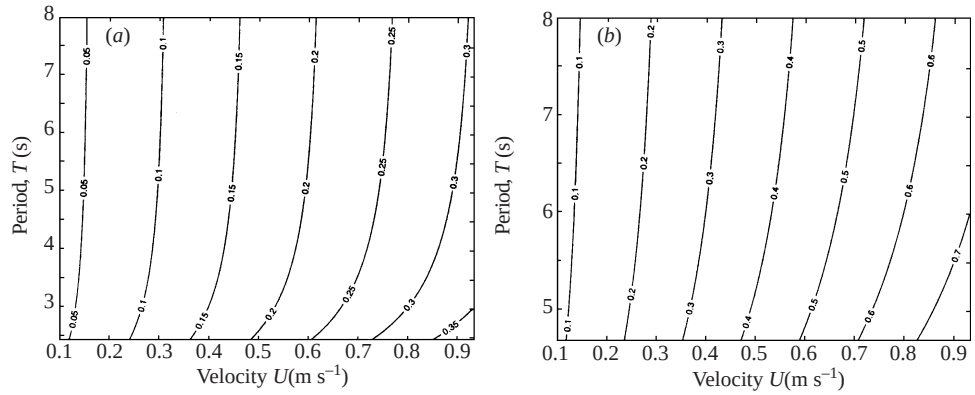

FIGURE 9. Contours of wave amplitude A (m) in water of depth (a) $h = 1.0$ m and (b) $h = 4.0$ m.

assumed to be travelling on the surface of a body of water of depth h. The relationship between the wave amplitude A, the wave period T and the orbital velocity U in the neighbourhood of the bottom is given by

$$A = \frac{1}{2\pi} T U \sinh(kh). \tag{5.7}$$

Using (5.6) and (5.7), we plot in figure 9 the dependence of the amplitude of the wave on the orbital velocity and the period for $h = 1$ m and $h = 4$ m. As expected, the deeper the water column, the higher the wave amplitude required to generate a lift that is comparable to, or bigger than, the gravitational force. From figures 8

τ	Min. lift	Max. lift	Left drag	Right drag
1.0000	−0.4271	−0.0521	−15.2481	15.2480
2.0000	−0.4444	0.0802	−7.9797	7.9796
3.0000	−0.4737	0.2093	−5.5148	5.5145
4.0000	−0.4939	0.3142	−4.2844	4.2841
5.0000	−0.4757	0.3930	−3.5557	3.5549
6.0000	−0.4384	0.4464	−3.0678	3.0665
7.0000	−0.3933	0.4821	−2.7274	2.7260
8.0000	−0.3434	0.5060	−2.4958	2.4941
10.0000	−0.2346	0.5302	−2.1857	2.1838
12.0000	−0.1341	0.5343	−1.9698	1.9697
14.0000	−0.0720	0.5281	−1.7996	1.7993
16.0000	−0.0456	0.5167	−1.6589	1.6596
24.0000	−0.0005	0.4601	−1.2852	1.2860
32.0000	0.0106	0.4171	−1.0672	1.0685
40.0000	0.0069	0.3894	−0.9627	0.9568
48.0000	−0.0011	0.3720	−0.9123	0.9056
56.0000	−0.0097	0.3583	−0.8748	0.8684
64.0000	−0.0185	0.3461	−0.8450	0.8385
72.0000	−0.0260	0.3349	−0.8205	0.8138
80.0000	−0.0327	0.3245	−0.7996	0.7928
96.0000	−0.0430	0.3062	−0.7648	0.7578

TABLE 6. For a given period τ, maximum and minimum lift over a cycle, maximum left and right drag over a cycle. $Re = 300$.

and 9, we can deduce the wave conditions required to lift a particle of a given size. For example, for a particle size of 0.85 mm and a period of 6 s, we see that a 15 cm wave would be required to have $R_{Lg} \approx 2$ in 1.0 m of water, whereas a 30 cm wave would be required in 4.0 m. The overall conclusion, as suggested by these estimates, is that lift forces can be important in the nearshore region, since waves of reasonable amplitude for this oceanic region can produce R_{Lg} values that easily reflect the importance of the lift force.

6. Concluding remarks

In this study, we computed the lift and drag force on a sphere resting on a smooth wall subjected to the oscillatory motion of an incompressible fluid over a Reynolds number range of 100–500. The data sets were obtained from simulations of the Navier–Stokes equations in three dimensions. These simulations were inspired by laboratory experiments in Rosenthal & Sleath (1986). In these experiments, the lift forces were obtained for particles that were of substantial size. Our simulations are aimed at extending the lift and drag data from the experiments to lower values of the Reynolds number, a flow regime in which RS report poor signal to noise ratios from their experimental rig.

The drag coefficient C_D obeys certain asymptotic characteristics, namely, a variation in magnitude that is inversely proportional to the Keulegan–Carpenter parameter τ, for small values of τ, and scales as $(Re\tau)^{-1/2}$ for large values of τ. The peak lift coefficient, C_L, was found to be negative for small values of τ, to climb to a maximum with increasing τ and to asymptotically decay at a rate faster than $(Re\tau)^{-1/2}$. This observation is consistent with an estimate due to Asmolov & McLaughlin (1999). Although this estimate is derived under the assumption that the particle is not

τ	Min. lift	Max. lift	Left drag	Right drag
1.0000	−0.5001	−0.0698	−14.7512	14.7509
2.0000	−0.5424	0.0698	−7.6517	7.6526
3.0000	−0.5913	0.2042	−5.2563	5.2555
4.0000	−0.5838	0.3204	−4.0841	4.0836
5.0000	−0.5547	0.4040	−3.3620	3.3610
6.0000	−0.5086	0.4617	−2.8771	2.8760
7.0000	−0.4578	0.5032	−2.5659	2.5635
8.0000	−0.3990	0.5308	−2.3691	2.3673
10.0000	−0.2589	0.5554	−2.0970	2.0962
12.0000	−0.1306	0.5535	−1.8986	1.8983
14.0000	−0.0953	0.5395	−1.7415	1.7404
16.0000	−0.0815	0.5239	−1.6041	1.6025
24.0000	0.0147	0.4624	−1.2348	1.2360
32.0000	0.0183	0.4001	−0.9991	1.0010
48.0000	0.0169	0.3552	−0.8319	0.8274
56.0000	0.0024	0.3413	−0.7964	0.7923
64.0000	−0.0067	0.3277	−0.7689	0.7647
72.0000	−0.0125	0.3164	−0.7466	0.7424
80.0000	−0.0175	0.3066	−0.7278	0.7237
96.0000	−0.0274	0.2899	−0.6972	0.6933
200.000	−0.0416	0.2394	−0.6199	0.6199

TABLE 7. For a given period τ, maximum and minimum lift over a cycle, maximum left and right drag over a cycle. $Re = 500$.

affected by the presence of a neighbouring wall, it provides a lower bound on the lift. The estimate states that, in the limit $\tau \to \infty$, the lift coefficient scales as $Re^{1/4}\tau^{-3/4}$.

RS report that C_L can reach values comparable to values of C_D. Our calculations do not support such a conclusion for the range of parameters considered. We do agree, however, with their assessment that the Keulegan–Carpenter number greatly influences the formation of vorticity, a crucial aspect of lift. This strong dependency inspired us to use τ, rather than the Reynolds number, as the main parameter in the calculations.

With the aid of extrapolation, we have also demonstrated that lift can be significant in the dynamics of sediment of the nearshore zone. However, as Cherukat & McLaughlin (1993) and Cherukat, McLaughlin & Graham (1994) report, particle rotation significantly affects the lift force on particles close to a solid surface. Although the flow regime and the type of flow considered in their study is different from the one under consideration here, it leads us to be more tentative about the significance of the lift force in the oceanic setting. A stronger conclusion will be made once our calculations on a freely moving particle in oscillatory boundary flow are analysed.

This work was supported by the Mathematical, Information, and Computational Sciences Division subprogram of the Office of Advanced Scientific Computing Research, US Department of Energy, under Contract W-31-109-Eng-38. We also thank the Faculty Research Participation program, administered by DEP, at Argonne National Laboratory, which was instrumental in enabling the collaboration that resulted in this study.

Appendix. Lift and drag data

Tables 5–7 give the raw data from the simulations.

REFERENCES

Acalar, M. S. & Smith, C. R. 1987 A study of hairpin vortices in a laminar boundary layer. Part 1. Hairpin vortices generated by a hemisphere protuberance. *J. Fluid Mech.* **175**, 1–41.

Asmolov, E. S. 1990 Dynamics of a spherical particle in a laminar boundary layer. *Fluid Dyn.* **25**, 886–890.

Asmolov, E. S. & McLaughlin, J. B. 1999 The inertial lift on an oscillating sphere in a linear shear flow. *Intl J. Multiphase Flow* **25**, 739–751.

Cherukat, P. & McLaughlin, J. B. 1993 The inertial lift on a rigid sphere in a linear shear-flow field near a flat wall, corrigendum. *J. Fluid Mech.* **263**, 1–18.

Cherukat, P., McLaughlin, J. B. & Graham, A. L. 1994 The intertial lift on a rigid sphere translating in a linear shear-flow field. *Intl J. Multiphase Flow* **20**, 339–353.

Cox, R. G. & Hsu, S. K. 1977 The lateral migration of solid particles in a laminar flow near a plane. *Intl J. Multiphase Flow* **3**, 201–222.

Dandy, D. & Dwyer, H. A. 1990 A sphere in shear flow at finite Reynolds number: effect of shear on particle lift, drag, and heat transfer. *J. Fluid Mech.* **216**, 381–410.

Dyer, K. R. & Soulsby, R. L. 1988 Sand transport on the continental shelf. *Annu Rev. Fluid Mech.* **20**, 295–324.

Fischer, P. F. 1997 An overlapping Schwarz method for spectral element solution of the incompressible Navier–Stokes equations. *J. Comput. Phys.* **133**, 84–101.

Fischer, P. F. & Mullen, J. S. 2001 Filter-based stabilization of spectral element methods. *C. R. Acad. Sci. Paris*, Série I – Analyse Numérique, **332**, 265–270.

Fredsøe, J. & Deigaard, R. 1992 *Mechanics of Coastal Sediment Transport*. World Scientific.

Hall, D. 1988 Measurements of the mean force on a particle near a boundary in turbulent flow. *J. Fluid Mech.* **187**, 451–466.

Harper, E. Y. & Chen, I. D. 1968 Maximum dissipation resulting from lift in a slow viscous shear flow. *J. Fluid Mech.* **33**, 209–225.

Honji, H. & Taneda, A. 1969 Unsteady flow past a circular cylinder. *J. Phys. Soc. Japan* **27**, 1668–1677.

Horikawa, K. 1981 Coastal sediment processes. *Annu. Rev. Fluid Mech.* **13**, 9–32.

Kim, I., Elghobashi, S. & Sirignano, W. 1998 On the equation of spherical-particle motion: effects of Reynolds and acceleration numbers. *J. Fluid Mech.* **367**, 221–253.

Kurose, R. & Komori, S. 1999 Drag and lift forces on a rotating sphere. *J. Fluid Mech.* **384**, 183–206.

Lovalenti, P. M. & Brady, J. F. 1995 The temporal behaviour of the hydrodynamic force on a body in response to an abrupt change in velocity at small but finite Reynolds number. *J. Fluid Mech.* **293**, 35–46.

McLaughlin, J. B. 1993 The lift on a small sphere in wall-bounded linear shear flows. *J. Fluid Mech.* **246**, 259–265.

Maday, Y. & Patera, A. T. 1989 Spectral element methods for the Navier–Stokes equations. In *State of the Art Surveys in Computational Mechanics* (ed. A. K. Noor), pp. 71–143. ASME.

Maday, Y. Patera, A. T. & Rønquist, E. M. 1990 An operator-integration-factor splitting method for time-dependent problems: application to incompressible fluid flow. *J. Sci. Comput.* **5**, 263–292.

Mollinger, A. M. & Nieuwstadt, F. T. M. 1996 Measurement of the lift force on a particle fixed to the wall in the viscous sublayer of a fully developed turbulent boundary layer. *J. Fluid Mech.* **316**, 285–306.

Nielsen, P. 1992 *Coastal Bottom Boundary Layers and Sediment Transport*. World Scientific.

Niño, Y. & Garcia, M. H. 1996 Experiments on particle-turbulence interactions in the near-wall region of an open channel flow: implications for sediment transport. *J. Fluid Mech.* **326**, 285–319.

Ponce-Campos, C. D. & Brater, E. 1985 Drag of oscillatory waves on spheres in a permeable bottom. *J. Waterway Port Coastal Ocean Engng ASCE* **111**, 45–61.

Restrepo, J. M. & Bona, J. L. 1995 Three-dimensional model for the formation of longshore sand ridges on the continental shelf. *Nonlinearity* **8**, 781–820.

Restrepo, J. M. 1997 Behaviour of a sand ridge model. *Euro. J. Mech. B/Fluids* **6**, 835–861.

Restrepo, J. M. 2001 Sediment dynamics and wave-current interactions. *Continental Shelf Res.* **21**, 1331–1360.

Rosenthal, G. & Sleath, J. 1986 Measurements of lift in oscillatory flow. *J. Fluid Mech.* **146**, 449–467.

Rubinov, S. I. & Keller, J. B. 1961 The transverse force on a spinning sphere moving in a viscous fluid. *J. Fluid Mech.* **11**, 447–459.

Saffman, P. G. 1965 The lift on a small sphere in a slow shear flow. *J. Fluid Mech.* **31**, 385–400.

Sakamoto, H. & Haniu, H. 1995 The formation mechanism and shedding frequency of vortices from a sphere in uniform shear flow. *J. Fluid Mech.* **287**, 151–171.

Sleath, J. 1984 *Sea Bed Mechanics.* Wiley Interscience.

Wang, Q., Squires, K., Chen, M. *et al.* 1997 On the role of the lift force in turbulence simulations of particle deposition. *Intl J. Multiphase Flow* **23**, 749–763.